

See discussions, stats, and author profiles for this publication at: <https://www.researchgate.net/publication/378216872>

A Fault Detection Algorithm for LiDAR/IMU Integrated Localization Systems with Non-Gaussian Noises

Conference Paper · February 2024

DOI: 10.33012/2024.19564

CITATIONS

0

READS

173

4 authors:



Penggao Yan
The Hong Kong Polytechnic University

10 PUBLICATIONS 129 CITATIONS

[SEE PROFILE](#)



Weisong Wen
The Hong Kong Polytechnic University

105 PUBLICATIONS 1,700 CITATIONS

[SEE PROFILE](#)



Feng Huang
The Hong Kong Polytechnic University

19 PUBLICATIONS 134 CITATIONS

[SEE PROFILE](#)



Li-Ta Hsu
The Hong Kong Polytechnic University

270 PUBLICATIONS 5,169 CITATIONS

[SEE PROFILE](#)

A Fault Detection Algorithm for LiDAR/IMU Integrated Localization Systems with Non-Gaussian Noises

Penggao Yan, Weisong Wen, Feng Huang and Li-Ta Hsu, *The Hong Kong Polytechnic University*

BIOGRAPHY

Penggao Yan is currently a Ph.D. candidate at the Hong Kong Polytechnic University. He received the bachelor's degree in Communication Engineering in 2018 and the master's degree in Pattern Recognition and Intelligent Systems in 2021, both from Wuhan University, China. His research interests include non-Gaussian noise modeling, fault detection and integrity monitoring in localization systems, and control-aided localization. He is also the winner of the ION Student Registration Grant, 2024.

Weisong Wen received the Ph.D. degree in mechanical engineering, The Hong Kong Polytechnic University. He was a Visiting Student Researcher at the University of California, Berkeley (UCB) in 2018. He is currently an Assistant Professor at the Department of Aeronautical and Aviation Engineering, Hong Kong Polytechnic University. His research interests include multi-sensor integrated localization for autonomous vehicles, SLAM, and GNSS positioning break in urban canyons.

Feng Huang received the bachelor's degree in automation from Shenzhen University, Shenzhen, China, in 2014, and the M.Sc. degree in electronic engineering from The Hong Kong University of Science and Technology, Hong Kong, in 2016. He is pursuing a Ph.D. degree with the Department of Aeronautical and Aviation Engineering, Hong Kong Polytechnic University, Hong Kong.

Li-Ta Hsu received the B.S. and Ph.D. degrees in aeronautics and astronautics from National Cheng Kung University, Taiwan, in 2007 and 2013, respectively. He is currently an assistant professor with the Division of Aeronautical and Aviation Engineering, Hong Kong Polytechnic University, before he served as post-doctoral researcher in Institute of Industrial Science at University of Tokyo, Japan. In 2012, he was a visiting scholar in University College London, U.K. He is an Associate Fellow of RIN. His research interests include GNSS positioning in challenging environments and localization for pedestrian, autonomous driving vehicle and unmanned aerial vehicle.

ABSTRACT

Fault detection for localization systems with non-Gaussian measurement noises is a challenging task. This paper investigates the impacts of noise modeling on fault detection performance in the inertial measurement units (IMU) and light detection and ranging (LiDAR) integrated localization system based on the extended Kalman filter (EKF). Specifically, we model the noise distribution of LiDAR range measurements as a Gaussian mixture model (GMM) and establish a clear relationship between the measurement noise and the measurement residual in EKF through error propagation. After proving that the measurement residual is also GMM distributed, a test statistic is constructed by transforming the measurement residual to a variable that approximates a standard multivariate normal (MVN) distribution based on the law of total covariance. Then, a Chi-squared test is performed based on the constructed test statistic to detect potential faults. The performance of the proposed method is evaluated in the simulated environment regarding two types of measurement failures, including the step failure and the slope failure. Compared to the method that adopts Gaussian noise modeling, the proposed method demonstrates its superiority in detecting small faults and the improved sensitivity to slowly increasing faults.

I. INTRODUCTION

Localization and navigation have become integral components of various commercial products, including autonomous vehicles and civil aviation. However, these systems face numerous challenges in terms of safety due to different types of faults that can occur. These faults encompass measurement errors resulting from sensor malfunctions, unusual system input/output dynamics, and malicious attacks on the system (Vargas et al., 2021). The consequences of such faults can be severe, leading to performance degradation or even catastrophic system failures. For example, global navigation satellite system (GNSS) measurements can be affected by many factors, such as multipath and non-line-of-sight (NLOS) issues (Kaplan & Hegarty, 2006). Light detection and ranging (LiDAR) measurements can be affected by adverse weather conditions such as rain, snowing, and fogging, leading to false detection of landmarks and the degradation of localization performance (Vargas Rivero et al., 2022). To ensure system integrity, the development of advanced fault detection algorithms is paramount, allowing for the timely identification and mitigation of faults, thus minimizing potential harm or disruptions to the overall system (Blanch et al., 2012; Walter & Enge,

1995).

Fault detection methods can be categorized into model-based, knowledge-based, and signal-based methods (Gao et al., 2015). Among these, model-based methods, particularly statistical analysis of residuals, are widely used for fault detection in localization and navigation systems (Pervan et al., 1998; Puchalski & Giernacki, 2022). However, conventional model-based methods typically assume Gaussian distribution for system noises (Joerger et al., 2014; Pervan et al., 1998), which is unrealistic for real-world applications. Recently, non-Gaussian noise modeling has garnered significant interest, with extensive exploration of its application in the localization and navigation domain, encompassing multi-sensor fusion, robust localization, and integrity monitoring (Davis & Blair, 2015; Rife, 2018). In these studies, the Gaussian mixture model (GMM) emerges as a popular approach for non-Gaussian noise modeling. However, there is limited research on fault detection considering GMM-based noise modeling. One example can be found in Yun et al., 2008, which developed a fault detection method using the Gaussian sum filter (GSF). In particular, the measurement noise is modeled as a GMM, and parallel Kalman filters are employed to handle each Gaussian component. The fault detection process involves comparing the one-side tail probability of the residual obtained from the GSF against a predefined threshold.

Recently, Hashemi and Ruths, 2019 proposed a fault detection method for linear time-invariant (LTI) control systems with non-Gaussian noise. They modeled the residual as a GMM and used the total mean and variance of the residual to construct test statistics for a Chi-squared test. This architecture is consistent with the conventional Gaussian method based on the Chi-squared test, providing valuable insights on fairly comparing the effects of non-Gaussian noise modeling on fault detection problems. Motivated by their work, this study aims to extend its idea to the fault detection problems in localization systems under non-Gaussian noises. Specifically, this study constructs a localization system by integrating 2D LiDAR measurements and inertial measurement units (IMU) measurements using extended Kalman filters (EKFs). The EKF linearization process is performed around the nominal state, making it possible to establish a clear relationship between the measurement noise and the measurement residual in EKF. Then, a fault detection algorithm based on the Chi-squared test is developed, where the test statistic is derived by transforming the measurement residual to a variable that approximates a standard multivariate normal (MVN) distribution based on the law of total covariance. A simulated urban environment is created using the 3D simulator CARLA (Dosovitskiy et al., 2017) to achieve fair comparisons between different detection algorithms. This allows for the simulation of GMM-distributed noises and ensures the reproducibility of experiments.

The performance of the proposed method is evaluated in the simulated environment regarding two types of measurement failures. In the step failure experiment, the fault detection rate of the proposed method outperforms the conventional Gaussian method by 30 %, highlighting the remarkable efficacy of the proposed approach in detecting minor faults. Moreover, in the slope failure experiment, the proposed method exhibits a notable reduction in detection delay of 17 % to 23 % compared to the Gaussian method, suggesting that the proposed method is more sensitive to faults with small magnitudes. The contribution of this study is twofold: 1) proposed a fault detection algorithm for an EKF-based localization system by modeling the non-Gaussian system and measurement noises as a Gaussian mixture model (GMM), where the measurement residual in EKF is proved to be the linear combination of the measurement noise and the process noise and is transformed to a normal variable for a Chi-squared test; 2) established a simulated urban environment based on the 3D simulator, CARLA, which provides a fault-free environment for LiDAR-based localization systems and enables the fault injection at specified period, allowing for fair comparisons of different fault detection algorithms under various failure scenarios.

II. LIDAR/IMU INTEGRATED LOCALIZATION SYSTEM

In this study, we construct a LiDAR/IMU integrated localization system by employing extended Kalman filters (Daum et al., 2005). The measurement function is established by matching the extracted line features from seven 2D LiDAR points to the plane in the prior map. Additionally, the state propagation equation is formed based on the kinematic model of the IMU motion. The state vector \mathbf{x} is defined as follows:

$$\mathbf{x} = [{}^G\mathbf{p}_I^T, {}^G\mathbf{v}_I^T, {}^I\mathbf{q}_G^T, \mathbf{b}_a^T, \mathbf{b}_g^T]^T, \quad (1)$$

with each element representing the position, velocity, rotation in terms of quaternion, bias of the accelerometer measurement, and bias of the gyroscope measurement in sequential order. Note that we use the notation ${}^G\mathbf{p}_I$ to represent the position of IMU frame ($\{I\}$) in the world frame ($\{G\}$), while using the notation ${}^I\mathbf{q}_G$ to represent the rotation from $\{G\}$ to $\{I\}$. The rotation matrix associated with ${}^I\mathbf{q}_G$ is denoted by ${}^I\mathbf{R}$. As shown in the sensor platform depicted in Figure 1, the world frame $\{G\}$ is fixed at the center of the pre-built point cloud map, adhering to the East-North-Up (ENU) coordinate system, while the IMU frame $\{I\}$ is affixed to the IMU. In addition, seven 2D LiDARs are placed at the top of the vehicle. Rather than defining separate frames for each of the seven 2D LiDARs, we define a single LiDAR frame $\{L\}$ fixed at the center of the fourth LiDAR. This approach allows us to present the main idea more clearly. Followed by this definition, we denote ${}^L\mathbf{p}_I$ as the translation from $\{I\}$ to $\{L\}$ and ${}^L\mathbf{q}_I$ as the rotation from $\{I\}$ to $\{L\}$. ${}^I\mathbf{p}_L$ and ${}^I\mathbf{R}$ are the extrinsic calibration parameters calibrated in the setup stage of the system based on the parameters provided in the embedded table in Figure 1.

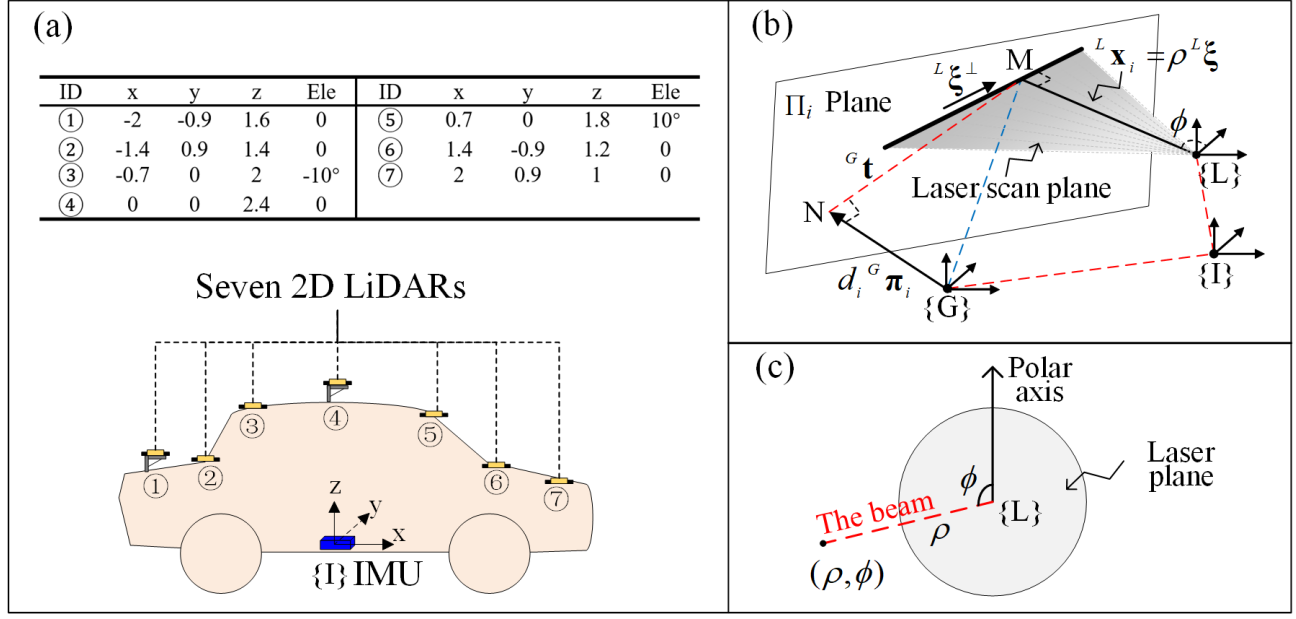


Figure 1: (a) The sensor platform of the localization system. The embedded table shows the center location and the elevation angle of each LiDAR in the IMU frame, where “Ele.” is the abbreviation of “Elevation angle”. (b) The 2D LiDAR measurement model is constructed by finding the shortest vector in the laser scan plane to the intersected line with the plane in $\{G\}$. (c) The laser plane in the polar coordinate system.

1. Motion Model of IMU

The kinematic model of the IMU motion in $\{G\}$ is adopted to propagate the vehicle state (Lefferts et al., 1982), and its discrete form can be written as follows:

$${}^G \mathbf{p}_{I,k+1} = {}^G \mathbf{p}_{I,k} + {}^G \mathbf{v}_{I,k} \Delta t + \frac{1}{2} \left({}_I \hat{\mathbf{R}} (\mathbf{a}_{m,k} - \mathbf{b}_{a,k} - \mathbf{n}_a) + {}^G \mathbf{g} \right) \Delta t^2 \quad (2a)$$

$${}^G \mathbf{v}_{I,k+1} = {}^G \mathbf{v}_{I,k} + \left({}_I \hat{\mathbf{R}} (\mathbf{a}_{m,k} - \mathbf{b}_{a,k} - \mathbf{n}_a) + {}^G \mathbf{g} \right) \Delta t \quad (2b)$$

$${}^I \mathbf{q}_{G,k+1} = \exp \left(\frac{\Delta t}{2} \boldsymbol{\Omega} [\mathbf{w}_{m,k} - \mathbf{b}_{g,k} - \mathbf{n}_g] \right) {}^I \mathbf{q}_{G,k} \quad (2c)$$

$$\mathbf{b}_{a,k+1} = \mathbf{b}_{a,k} + \mathbf{n}_{wa} \Delta t \quad (2d)$$

$$\mathbf{b}_{g,k+1} = \mathbf{b}_{g,k} + \mathbf{n}_{wg} \Delta t, \quad (2e)$$

where Δt is a short time period; ${}_I \hat{\mathbf{R}}$ represents the estimation of the vehicle orientation at time k ; $\mathbf{a}_{m,k}$ and $\mathbf{b}_{a,k}$ are the acceleration measurement and the associated bias at time k , respectively; \mathbf{n}_a is the noise of the accelerator measurement with covariance Σ_a ; ${}^G \mathbf{g}$ is the gravitational acceleration; $\mathbf{w}_{m,k}$ and $\mathbf{b}_{g,k}$ are the gyroscope measurement and the associated bias at time k , respectively; \mathbf{n}_g is the noise of the gyroscope measurement with covariance Σ_g ; \mathbf{n}_{wa} and \mathbf{n}_{wg} are zero-mean Gaussian white noise whose covariance are denoted as Σ_{wa} and Σ_{wg} , respectively; $\boldsymbol{\Omega}[\cdot]$ is a 4×4 skew symmetric matrix and $\exp(\cdot)$ is a function of matrix defined by

$$\exp(\mathbf{M}) = \sum_{i=0}^n \frac{\mathbf{M}^n}{n!}. \quad (3)$$

The linearization of Equation (2c) is given by

$${}^I \mathbf{q}_{G,k+1} = \mathbf{S}_1 {}^I \mathbf{q}_{G,k} + \mathbf{S}_2 (\mathbf{w}_{m,k} - \mathbf{b}_{g,k} - \mathbf{n}_g), \quad (4)$$

where

$$\begin{aligned}\mathbf{S}_1 &= \begin{bmatrix} \mathbf{I}_3 - \frac{1}{2}\Delta t [\mathbf{w}_{m,k} - \mathbf{b}_{g,k} - \mathbf{n}_g]_{\times} & \frac{1}{2}\Delta t (\mathbf{w}_{m,k} - \mathbf{b}_{g,k} - \mathbf{n}_g) \\ -\frac{1}{2}\Delta t (\mathbf{w}_{m,k} - \mathbf{b}_{g,k} - \mathbf{n}_g)^T & 1 \end{bmatrix} \\ \mathbf{S}_2 &= \frac{\Delta t}{2} \begin{bmatrix} \hat{q}_{z,k} & -\hat{q}_{y,k} & \hat{q}_{x,k} \\ \hat{q}_{y,k} & \hat{q}_{z,k} & -\hat{q}_{w,k} \\ -\hat{q}_{x,k} & \hat{q}_{w,k} & \hat{q}_{z,k} \\ -\hat{q}_{w,k} & -\hat{q}_{x,k} & -\hat{q}_{y,k} \end{bmatrix},\end{aligned}\quad (5)$$

${}^I\hat{\mathbf{q}}_{G,k} = [\hat{q}_{w,k}, \hat{q}_{x,k}, \hat{q}_{y,k}, \hat{q}_{z,k}]$ is the estimated vehicle orientation in terms of quaternion at time k , and $[\cdot]_{\times}$ denotes the standard vector cross-product.

2. 2D LiDAR Measurement Model

The basic idea of the 2D LiDAR measurement model (Hesch et al., 2010; Zhao & Farrell, 2013) is illustrated in Figure 1(b). Assuming that the laser scan plane is intersected with the plane Π_i at line ${}^L\xi_i^{\perp}$ in $\{L\}$, we can find the shortest vector ${}^L\mathbf{x}_i = \rho_i {}^L\xi_i$ in the LiDAR scan plane from the origin of $\{L\}$ to Π_i , where ${}^L\xi_i$ is the unit vector, ρ_i is the length of ${}^L\mathbf{x}_i$, and the point M is the intersection of ${}^L\mathbf{x}_i$ and ${}^L\xi_i^{\perp}$. The laser beam ${}^L\mathbf{x}_i$ in the scan laser plane can be represented by ranging and bearing parameters (ρ_i, ϕ_i) in the polar coordinate system, as shown in Figure 1(c). Alternatively, ${}^L\mathbf{x}_i$ can also be written as ${}^L\mathbf{x}_i = [\rho_i \cos \phi_i \ \rho_i \sin \phi_i \ 0]^T$ in $\{L\}$. The shortest vector from the origin of $\{G\}$ to the plane Π_i is denoted by $d_i {}^G\boldsymbol{\pi}_i$ and is intersected with Π_i at point N, where ${}^G\boldsymbol{\pi}_i$ is the normal of the plane in $\{G\}$ and d_i is the length of $d_i {}^G\boldsymbol{\pi}_i$. The vector from M to N in $\{G\}$ is denoted by ${}^G\mathbf{t}_i$. Assuming that the extrinsic calibration parameters $({}^I\mathbf{p}_L, {}^I_L\mathbf{R})$ and the vehicle pose $({}^G\mathbf{p}_I, {}^G\mathbf{R})$ are known, the plane Π_i associated with the current LiDAR scan plan is found based on the vehicle pose $({}^G\mathbf{p}_I, {}^G\mathbf{R})$ by a matching algorithm, and d_i and ${}^G\boldsymbol{\pi}_i$ are known, we have following constraints:

(1) ${}^L\mathbf{x}_i$ is a laser beam so that it must be in the LiDAR scan plane (Zhao & Farrell, 2013)

Let ${}^L\mathbf{z}_L = [0 \ 0 \ 1]^T$ be the normal of the LiDAR scan plane, we have

$${}^L\mathbf{z}_L^T {}^L\mathbf{x}_i = 0. \quad (6)$$

(2) Distance constraint (Hesch et al., 2010)

As can be seen in Figure 1(c), the vector from $\{G\}$ to point M can be obtained either by

$${}^G\mathbf{p}_I + {}^G_I\mathbf{R} ({}^I\mathbf{p}_L + {}^I_L\mathbf{R} {}^L\mathbf{x}_i) \quad (7)$$

or

$$d_i {}^G\boldsymbol{\pi}_i + {}^G\mathbf{t}_i, \quad (8)$$

both of which are equivalent. Therefore, we have

$${}^G\mathbf{p}_I + {}^G_I\mathbf{R} ({}^I\mathbf{p}_L + {}^I_L\mathbf{R} {}^L\mathbf{x}_i) = d_i {}^G\boldsymbol{\pi}_i + {}^G\mathbf{t}_i. \quad (9)$$

The shortest ${}^L\mathbf{x}_i$ satisfying Equations (6) and (9) can be solved by a least-norm optimization problem. The optimal solution is

$$\phi_i^* = \arctan \left(\operatorname{sgn} ({}^L d_i) \frac{a_2^i}{a_1^i} \right) \quad (10a)$$

$$\rho_i^* = \frac{|{}^L d_i|}{\sqrt{{a_1^i}^2 + {a_2^i}^2}}, \quad (10b)$$

where $\operatorname{sgn}(\cdot)$ is the sign function, and

$${}^L d_i = d_i - {}^G\boldsymbol{\pi}_i^T ({}^G\mathbf{p}_I + {}^G_I\mathbf{R} {}^I\mathbf{p}_L) \quad (11a)$$

$${}^L \mathbf{a}_i = {}^G_I\mathbf{R} {}^G\boldsymbol{\pi}_i = [a_1^i, a_2^i, a_3^i]^T. \quad (11b)$$

Denote the i th measurement of the LiDAR at time k as $\mathbf{y}_{i,k} = [\phi_{i,k}, \rho_{i,k}]^T$, which is the ranging and bearing parameters associated with the shortest vector in the laser plane intersected with Π_i . Then, the LiDAR measurement model at time k can be written as

$$\phi_{i,k} = h_1^i(\mathbf{x}_k) + \tilde{\phi}_{i,k} = \arctan \left(\operatorname{sgn}(^L d_{i,k}) \frac{a_2^{i,k}}{a_1^{i,k}} \right) + \tilde{\phi}_{i,k} \quad (12a)$$

$$\rho_{i,k} = h_2^i(\mathbf{x}_k) + \tilde{\rho}_{i,k} = \frac{|^L d_{i,k}|}{\sqrt{a_1^{i,k}{}^2 + a_2^{i,k}{}^2}} + \tilde{\rho}_{i,k}, \quad (12b)$$

where $\tilde{\phi}_{i,k}$ and $\tilde{\rho}_{i,k}$ are measurement noises, $^L d_{i,k}$ and $^L \mathbf{a}_{i,k} = [a_1^{i,k}, a_2^{i,k}, a_3^{i,k}]^T$ are the discrete version of $^L d_i$ and $^L \mathbf{a}_i$ at time k . Let

$$\mathbf{y}_{i,k} = \begin{bmatrix} \phi_{i,k} \\ \rho_{i,k} \end{bmatrix}, h^i(\mathbf{x}) = \begin{bmatrix} h_1^i(\mathbf{x}) \\ h_2^i(\mathbf{x}) \end{bmatrix}, \boldsymbol{\eta}_{i,k} = \begin{bmatrix} \tilde{\phi}_{i,k} \\ \tilde{\rho}_{i,k} \end{bmatrix}. \quad (13)$$

The measurement model takes the standard form as follows:

$$\mathbf{y}_{i,k} = h^i(\mathbf{x}_k) + \boldsymbol{\eta}_{i,k}. \quad (14)$$

Since $h^i(\mathbf{x}_k)$ is a non-linear function of \mathbf{x}_k , as shown in Equation (12), the linearization of $h^i(\mathbf{x}_k)$ is required to accommodate the EKF. Let $\hat{\mathbf{x}}_k^- = [{}^G \hat{\mathbf{p}}_I^{-T}, {}^G \mathbf{v}_I^{-T}, {}^I \hat{\mathbf{q}}_G^{-T}, \hat{\mathbf{b}}_a^T, \hat{\mathbf{b}}_g^T]^T$ be the predicted state at time k , and \mathbf{H}_k^i be the Jacobian matrix of $h^i(\mathbf{x}_k)$ defined with respect to \mathbf{x}_k and evaluated at $\hat{\mathbf{x}}_k^-$. Then, we have:

$$\mathbf{H}_k^i = \frac{\partial h^i(\hat{\mathbf{x}}_k^-)}{\partial \mathbf{x}_k} = \begin{bmatrix} \frac{\partial h_1^i(\hat{\mathbf{x}}_k^-)}{\partial {}^G \mathbf{p}_I} & 0_{1 \times 3} & \frac{\partial h_1^i(\hat{\mathbf{x}}_k^-)}{\partial {}^I \mathbf{q}_G} & 0_{1 \times 6} \\ \frac{\partial h_2^i(\hat{\mathbf{x}}_k^-)}{\partial {}^G \mathbf{p}_I} & 0_{1 \times 3} & \frac{\partial h_2^i(\hat{\mathbf{x}}_k^-)}{\partial {}^I \mathbf{q}_G} & 0_{1 \times 6} \end{bmatrix}. \quad (15)$$

Equation (15) contains the derivative of rotation matrices, which can be solved by taking the derivative elementwise. Through calculation, the finalized Jacobin matrix is given by

$$\mathbf{H}_k^i = \begin{bmatrix} 0_{1 \times 3} & 0_{1 \times 3} & \frac{1}{\hat{\mu}_{i,k}^-} \hat{\lambda}_{i,k}^{-T} {}^L \mathbf{R} J_q^*({}^I \hat{\mathbf{q}}_G^-, {}^G \boldsymbol{\pi}_{i,k}) & 0_{1 \times 6} \\ -\operatorname{sgn}({}^L \hat{d}_{i,k}^-) \frac{{}^G \boldsymbol{\pi}_{i,k}^T}{\sqrt{\hat{\mu}_{i,k}^-}} & 0_{1 \times 3} & -\operatorname{sgn}({}^L \hat{d}_{i,k}^-) \frac{{}^G \boldsymbol{\pi}_{i,k}^T}{\sqrt{\hat{\mu}_{i,k}^-}} J_q({}^I \hat{\mathbf{q}}_G^-, {}^I \mathbf{p}_L) + |{}^L \hat{d}_{i,k}^-| \hat{\kappa}_{i,k}^T {}^L \mathbf{R} J_q^*({}^I \hat{\mathbf{q}}_G^-, {}^G \boldsymbol{\pi}_{i,k}) & 0_{1 \times 6} \end{bmatrix}, \quad (16)$$

where

$$\begin{aligned} \hat{\mu}_{i,k}^- &= a_1^{i,k-2} + a_2^{i,k-2}, \boldsymbol{\lambda}_{i,k}^- = \operatorname{sgn}({}^L \hat{d}_{i,k}^-) [-\hat{a}_2^{i,k-}, \hat{a}_1^{i,k-}, 0], \\ \hat{\kappa}_{i,k}^T &= -\hat{\mu}_{i,k}^{-\frac{3}{2}} [\hat{a}_1^{i,k-}, \hat{a}_2^{i,k-}, 0], {}^I \hat{\mathbf{a}}_{i,k}^- = {}^I \mathbf{R}_G^T \hat{\mathbf{R}} {}^G \boldsymbol{\pi}_{i,k} = [\hat{a}_1^{i,k-}, \hat{a}_2^{i,k-}, \hat{a}_3^{i,k-}]^T, \\ J_q({}^I \hat{\mathbf{q}}_G^-, {}^I \mathbf{p}_L) &= 2 \left[[{}^I \mathbf{p}_L] \times {}^I \hat{\mathbf{q}}_{G,v}^- \left[[{}^I \mathbf{p}_L] \times {}^I \hat{\mathbf{q}}_{G,v}^- + {}^I \hat{\mathbf{q}}_{G,w}^- {}^I \mathbf{p}_L \right] \right] + \left({}^I \hat{\mathbf{q}}_{G,v}^- \cdot {}^I \mathbf{p}_L \right) \mathbf{I}_3 - {}^I \mathbf{p}_L {}^I \hat{\mathbf{q}}_{G,v}^{-T}, \\ J_q^*({}^I \hat{\mathbf{q}}_G^-, {}^G \boldsymbol{\pi}_{i,k}) &= J_q \left({}^I \hat{\mathbf{q}}_G^{*-}, {}^G \boldsymbol{\pi}_{i,k} \right) \operatorname{diag}[1, -1, -1, -1], \end{aligned} \quad (17)$$

and ${}^I \hat{\mathbf{q}}_G^{*-}$ is the conjugate of ${}^I \hat{\mathbf{q}}_G^-$. For multiple measurements $\mathbf{y}_k = [\mathbf{y}_{1,k}^T, \mathbf{y}_{2,k}^T, \dots, \mathbf{y}_{n,k}^T]^T$ at time k , the measurement function is written as

$$\mathbf{y}_k = h(\mathbf{x}_k) + \boldsymbol{\eta}_k, \quad (18)$$

where

$$h(\mathbf{x}_k) = [h^1(\mathbf{x}_k)^T, h^2(\mathbf{x}_k)^T, \dots, h^n(\mathbf{x}_k)^T]^T \quad (19a)$$

$$\boldsymbol{\eta}_k = [\boldsymbol{\eta}_{1,k}^T, \boldsymbol{\eta}_{2,k}^T, \dots, \boldsymbol{\eta}_{n,k}^T]^T, \quad (19b)$$

and n is the total number of measurements at time k . Then the Jacobian matrix of $h(\mathbf{x}_k)$ can be written as

$$\mathbf{H}_k^T = \left[\mathbf{H}_k^{1T}, \mathbf{H}_k^{2T}, \dots, \mathbf{H}_k^{nT} \right]^T. \quad (20)$$

It is worth noting that the linearization process presented here is quite different from the work of Hesch et al. (2010) and Zhao and Farrell (2013). In this work, we linearize the measurement function at the nominal state. This method, as demonstrated in Equation (15), offers a more straightforward and intuitive approach compared to the approach that performs linearization at the error state (Hesch et al., 2010; Zhao & Farrell, 2013). In addition, linearization at the nominal state can help establish a distinct correspondence between the measurement noise and the state, as well as the relationship between the measurement noise and the residual. These benefits are illustrated in Section III.1.

3. LiDAR/IMU Integration Based on EKF

By summarizing the derivations in Section II.1, the discrete-time state propagation equation can be summarized as:

$$\mathbf{x}_k = f(\mathbf{x}_{k-1}, \mathbf{u}_{k-1}, \mathbf{v}_{k-1}), \quad (21)$$

where $\mathbf{v}_{k-1} = [\mathbf{n}_a^T, \mathbf{n}_g^T, \mathbf{n}_{wa}^T, \mathbf{n}_{wg}^T]^T$ is the process noise at time $k-1$, and $\mathbf{u}_{k-1} = [\mathbf{a}_{m,k-1}^T, \mathbf{w}_{m,k-1}^T]^T$ is the external input which is the readings from the IMU at time $k-1$. Then, the propagation equations are yielded as follows:

$$\hat{\mathbf{x}}_k^- = f(\hat{\mathbf{x}}_{k-1}^+, \mathbf{u}_{k-1}, 0) \quad (22a)$$

$$\mathbf{P}_k^- = \mathbf{F}_{k-1} \mathbf{P}_{k-1} \mathbf{F}_{k-1}^T + \mathbf{G}_{k-1} \mathbf{Q}_{k-1} \mathbf{G}_{k-1}^T, \quad (22b)$$

where $\hat{\mathbf{x}}_{k-1}^+$ is the estimated state at time $k-1$, $\hat{\mathbf{x}}_k^-$ is the predicted state at time k , \mathbf{P}_{k-1} is the covariance matrix of the estimated state by the EKF at time $k-1$, \mathbf{P}_k^- is the predicted covariance matrix of the estimated state at time k , and \mathbf{F}_{k-1} is the 15×15 state transition matrix at time $k-1$,

$$\mathbf{F}_{k-1} = \begin{bmatrix} \mathbf{I}_3 & \mathbf{I}_3 \Delta t & 0 & -\frac{1}{2} \hat{\mathbf{R}} \Delta t^2 & 0 \\ 0 & \mathbf{I}_3 & 0 & -\frac{G}{I} \hat{\mathbf{R}} \Delta t & 0 \\ 0 & 0 & \mathbf{S}_1 & 0 & -\mathbf{S}_2 \\ 0 & 0 & 0 & \mathbf{I}_3 & 0 \\ 0 & 0 & 0 & 0 & \mathbf{I}_3 \end{bmatrix}, \quad (23)$$

\mathbf{G}_{k-1} is the 15×12 noise Jacobian matrix at time $k-1$,

$$\mathbf{G}_{k-1} = \begin{bmatrix} -\frac{1}{2} \hat{\mathbf{R}} \Delta t^2 & 0 & 0 & 0 \\ -\frac{G}{I} \hat{\mathbf{R}} \Delta t & 0 & 0 & 0 \\ 0 & -\mathbf{S}_2 & 0 & 0 \\ 0 & 0 & \mathbf{I}_3 \Delta t & 0 \\ 0 & 0 & 0 & \mathbf{I}_3 \Delta t \end{bmatrix}, \quad (24)$$

and \mathbf{Q}_{k-1} is the covariance matrix of \mathbf{v}_{k-1} , which is set as

$$\mathbf{Q}_{k-1} = \text{diag}(\Sigma_a, \Sigma_g, \Sigma_{wa}, \Sigma_{wg}). \quad (25)$$

If the EKF receives measurements \mathbf{y}_k at time k , the Kalman gain \mathbf{K}_k is obtained by the following equation (Daum, 2005):

$$\mathbf{K}_k = \mathbf{P}_k^- \mathbf{H}_k^T (\mathbf{H}_k \mathbf{P}_k^- \mathbf{H}_k^T + \mathbf{R}_k)^{-1}, \quad (26)$$

and the estimated state at time k is obtained by

$$\hat{\mathbf{x}}_k^+ = \hat{\mathbf{x}}_k^- + \mathbf{K}_k (\mathbf{y}_k - h(\hat{\mathbf{x}}_k^-)), \quad (27)$$

where $h(\cdot)$ is the measurement function defined in Equation (19a). The covariance of the estimated state is given by

$$\mathbf{P}_k = (\mathbf{I} - \mathbf{K}_k \mathbf{H}_k) \mathbf{P}_k^- . \quad (28)$$

III. FAULT DETECTION BASED ON GMM NOISE MODELING

1. Analysis of Measurement Residual

The residual corresponding to the measurements at time k is

$$\mathbf{r}_k = \mathbf{y}_k - h(\hat{\mathbf{x}}_k^-) . \quad (29)$$

By substituting Equation (18) into Equation (29) and taking the first-order Taylor expansion at $\hat{\mathbf{x}}_k^-$, we can obtain

$$\mathbf{r}_k = \mathbf{H}_k (\mathbf{x}_k - \hat{\mathbf{x}}_k^-) + \boldsymbol{\eta}_k . \quad (30)$$

Substitute Equations (21) and (22a) into Equation (30) and apply the first-order Taylor expansion at the point $(\hat{\mathbf{x}}_{k-1}^+, 0)$,

$$\mathbf{r}_k = \mathbf{H}_k (\mathbf{F}_{k-1} (\mathbf{x}_{k-1} - \hat{\mathbf{x}}_{k-1}^+) + \mathbf{G}_{k-1} \mathbf{v}_{k-1}) + \boldsymbol{\eta}_k . \quad (31)$$

Assume that $\hat{\mathbf{x}}_{k-1}^+$ is obtained by the state propagation (In general, the update frequency of IMU is much higher than that of LiDAR), we have

$$\mathbf{x}_{k-1} - \hat{\mathbf{x}}_{k-1}^+ = \mathbf{x}_{k-1} - \hat{\mathbf{x}}_{k-1}^- . \quad (32)$$

Substitute Equations (21) and (22a) into Equation (32) and take the first-order Taylor expansion at $(\hat{\mathbf{x}}_{k-2}^+, \mathbf{u}_{k-2}, 0)$,

$$\mathbf{x}_{k-1} - \hat{\mathbf{x}}_{k-1}^+ = \mathbf{F}_{k-2} (\mathbf{x}_{k-2} - \hat{\mathbf{x}}_{k-2}^+) + \mathbf{G}_{k-2} \mathbf{v}_{k-2} . \quad (33)$$

Repeat the operation in Equations (31)–(33), we have

$$\mathbf{r}_k = \mathbf{H}_k \left(\prod_{i=1}^m \mathbf{F}_{k-i} (\mathbf{x}_{k-m} - \hat{\mathbf{x}}_{k-m}^+) + \sum_{i=2}^m \prod_{j=1}^{i-1} \mathbf{F}_{k-j} \mathbf{G}_{k-i} \mathbf{v}_{k-i} + \mathbf{G}_{k-1} \mathbf{v}_{k-1} \right) + \boldsymbol{\eta}_k , \quad (34)$$

where m is the discrete time interval between the last and the current measurements. To focus on the development of the fault detection algorithm, we set the higher-order terms (>2) to zero and obtain

$$\mathbf{r}_k = \mathbf{H}_k \mathbf{F}_{k-1} \mathbf{G}_{k-2} \mathbf{v}_{k-2} + \mathbf{H}_k \mathbf{G}_{k-1} \mathbf{v}_{k-1} + \boldsymbol{\eta}_k . \quad (35)$$

Let

$$\mathbf{V}_{k-1} = \mathbf{H}_k \mathbf{G}_{k-1} , \quad (36)$$

and

$$\mathbf{N}_{k-1} = \mathbf{H}_k \mathbf{F}_{k-1} \mathbf{G}_{k-2} . \quad (37)$$

Then Equation (35) can be written as

$$\mathbf{r}_k = \mathbf{V}_{k-1} \mathbf{v}_{k-1} + \mathbf{N}_{k-1} \mathbf{v}_{k-2} + \boldsymbol{\eta}_k . \quad (38)$$

In this study, \mathbf{v}_{k-1} , \mathbf{v}_{k-2} , and $\boldsymbol{\eta}_k$ are assumed to be non-Gaussian noises, and we use the multivariate GMM to model them. Assuming \mathbf{v}_{k-1} and \mathbf{v}_{k-2} are independent and identically distributed (i.i.d.), we can obtain the PDF of $\boldsymbol{\eta}$ and \mathbf{v} by

$$f_{\boldsymbol{\eta}}(\mathbf{x}) = \sum_{j=1}^{m_1} p_j^\eta \mathcal{N}(\mathbf{x} | \boldsymbol{\mu}_j^\eta, \boldsymbol{\pi}_j^\eta) \quad (39a)$$

$$f_{\mathbf{v}}(\mathbf{x}) = \sum_{j=1}^{m_2} p_j^v \mathcal{N}(\mathbf{x} | \boldsymbol{\mu}_j^v, \boldsymbol{\pi}_j^v) , \quad (39b)$$

where $\sum_{j=1}^{m_1} p_j^\eta = 1$, $\sum_{j=1}^{m_2} p_j^v = 1$; m_1 and m_2 are the number of Gaussian modes for $\boldsymbol{\eta}$ and \mathbf{v} , respectively; p_j^η and p_j^v are the mixture weight (i.e., the prior probability of each Gaussian mode); $\mathcal{N}(\cdot | \boldsymbol{\mu}_j^\eta, \boldsymbol{\pi}_j^\eta)$ and $\mathcal{N}(\cdot | \boldsymbol{\mu}_j^v, \boldsymbol{\pi}_j^v)$ are probability density

functions of each Gaussian mode; $\boldsymbol{\mu}_j^\eta \in \mathbb{R}^{2n}$ and $\boldsymbol{\mu}_j^v \in \mathbb{R}^{12}$ are means of each Gaussian mode; $\boldsymbol{\pi}_j^\eta \in \mathbb{R}^{2n \times 2n}$ and $\boldsymbol{\pi}_j^v \in \mathbb{R}^{12 \times 12}$ are covariance matrixes of each Gaussian mode; and n is the number of measurements.

Inspired by the work of Hashemi and Ruths (2019), it can be proved that \mathbf{r}_k follows a multivariate Gaussian mixture model (GMM) distribution. This can be achieved by applying the convolution theorem to the characteristic function of each residual component. Specifically, since \mathbf{r}_k is the linear combination of independent random variables $\mathbf{V}_{k-1}\mathbf{v}_{k-1}$, $\mathbf{N}_{k-1}\mathbf{v}_{k-2}$, and $\boldsymbol{\eta}_k$, the PDF of \mathbf{r}_k is the convolution of the PDF of these random variables, which can be written as

$$f_{\mathbf{r}_k} = f_{\mathbf{V}_{k-1}\mathbf{v}} * f_{\mathbf{N}_{k-1}\mathbf{v}} * f_{\boldsymbol{\eta}_k}, \quad (40)$$

where $*$ is the convolution operator. Since \mathbf{v}_{k-1} and \mathbf{v}_{k-2} are assumed to be i.i.d., we drop the time index in the above equation. The characteristic functions of \mathbf{r}_k , $\boldsymbol{\eta}_k$, and \mathbf{v} are given as follows:

$$\varphi_{\mathbf{r}_k}(\omega) = \int_{-\infty}^{\infty} f_{\mathbf{r}_k}(\mathbf{x}) e^{i\omega^T \mathbf{x}} d\mathbf{x} \quad (41a)$$

$$\begin{aligned} \varphi_{\boldsymbol{\eta}}(\omega) &= \int_{-\infty}^{\infty} f_{\boldsymbol{\eta}}(\mathbf{x}) e^{i\omega^T \mathbf{x}} d\mathbf{x} = \sum_{j=1}^{m_1} p_j^\eta \int_{-\infty}^{\infty} \mathcal{N}(\mathbf{x} | \boldsymbol{\mu}_j^\eta, \boldsymbol{\pi}_j^\eta) e^{i\omega^T \mathbf{x}} d\mathbf{x} \\ &= \sum_{j=1}^{m_1} p_j^\eta \varphi_{\mathcal{N}}(\omega) = \sum_{j=1}^{m_1} p_j^\eta e^{i\omega^T \boldsymbol{\mu}_j^\eta - \frac{1}{2} \omega^T \boldsymbol{\pi}_j^\eta \omega} \end{aligned} \quad (41b)$$

$$\begin{aligned} \varphi_{\mathbf{v}}(\omega) &= \int_{-\infty}^{\infty} f_{\mathbf{v}}(\mathbf{x}) e^{i\omega^T \mathbf{x}} d\mathbf{x} = \sum_{j=1}^{m_2} p_j^v e^{i\omega^T \boldsymbol{\mu}_j^v - \frac{1}{2} \omega^T \boldsymbol{\pi}_j^v \omega}, \end{aligned} \quad (41c)$$

where $\varphi_{\mathcal{N}}(\omega)$ is the characteristic function of a multinormal variable. Let $\mathbf{y} = \mathbf{Ax} + \mathbf{b}$ be the linear transformation of the random vector \mathbf{x} , where \mathbf{A} is a constant matrix and \mathbf{b} is a constant vector. The characteristic function of \mathbf{y} is given by

$$\varphi_{\mathbf{y}}(\omega) = e^{i\omega^T \mathbf{b}} \varphi_{\mathbf{x}}(\mathbf{A}^T \omega). \quad (42)$$

Therefore, we have

$$\varphi_{\mathbf{N}_{k-1}\mathbf{v}}(\omega) = \varphi_{\mathbf{v}}(\mathbf{N}_{k-1}^T \omega) = \sum_{j=1}^{m_2} p_j^v e^{i\omega^T \mathbf{N}_{k-1} \boldsymbol{\mu}_j^v - \frac{1}{2} \omega^T \mathbf{N}_{k-1} \boldsymbol{\pi}_j^v \mathbf{N}_{k-1}^T \omega} \quad (43a)$$

$$\varphi_{\mathbf{V}_{k-1}\mathbf{v}}(\omega) = \varphi_{\mathbf{v}}(\mathbf{V}_{k-1}^T \omega) = \sum_{j=1}^{m_2} p_j^v e^{i\omega^T \mathbf{V}_{k-1} \boldsymbol{\mu}_j^v - \frac{1}{2} \omega^T \mathbf{V}_{k-1} \boldsymbol{\pi}_j^v \mathbf{V}_{k-1}^T \omega}. \quad (43b)$$

According to the convolution theorem,

$$\varphi_{\mathbf{r}_k}(\omega) = \varphi_{\mathbf{v}}(\mathbf{V}_{k-1}^T \omega) \cdot \varphi_{\mathbf{v}}(\mathbf{N}_{k-1}^T \omega) \cdot \varphi_{\boldsymbol{\eta}}(\omega), \quad (44)$$

where \cdot is point-wise multiplication. Substituting Equations (41b) and (43) into Equation (44), we can obtain

$$\varphi_{\mathbf{r}_k}(\omega) = \sum_{a=1}^{m_2} \sum_{b=1}^{m_2} \sum_{c=1}^{m_1} p_{abc} e^{i\omega^T \boldsymbol{\mu}_{abc} - \frac{1}{2} \omega^T \boldsymbol{\pi}_{abc} \omega}, \quad (45)$$

where

$$p_{abc} = p_a^v p_b^v p_c^\eta \quad (46a)$$

$$\boldsymbol{\mu}_{abc} = \mathbf{V}_{k-1} \boldsymbol{\mu}_a^v + \mathbf{N}_{k-1} \boldsymbol{\mu}_b^v + \boldsymbol{\mu}_c^\eta \quad (46b)$$

$$\boldsymbol{\pi}_{abc} = \mathbf{V}_{k-1} \boldsymbol{\pi}_a^v \mathbf{V}_{k-1}^T + \mathbf{N}_{k-1} \boldsymbol{\pi}_b^v \mathbf{N}_{k-1}^T + \boldsymbol{\pi}_c^\eta. \quad (46c)$$

Do the inverse operation shown in Equation (41b),

$$\varphi_{\mathbf{r}_k}(\omega) = \sum_{a=1}^{m_2} \sum_{b=1}^{m_2} \sum_{c=1}^{m_1} p_{abc} \int_{-\infty}^{\infty} \mathcal{N}(\mathbf{x}|\boldsymbol{\mu}_{abc}, \boldsymbol{\pi}_{abc}) e^{i\omega^T \mathbf{x}} d\mathbf{x}. \quad (47)$$

Therefore,

$$f_{\mathbf{r}_k}(\mathbf{x}) = \sum_{a=1}^{m_2} \sum_{b=1}^{m_2} \sum_{c=1}^{m_1} p_{abc} \mathcal{N}(\mathbf{x}|\boldsymbol{\mu}_{abc}, \boldsymbol{\pi}_{abc}) d\mathbf{x}, \quad (48)$$

which indicates that \mathbf{r}_k has a multivariate GMM distribution.

2. Chi-Squared Test Based on Residual Transformation

Section III.1 illustrates that the residual is a multivariate GMM distributed random variable. To align with the architecture of the Chi-squared detector, we transform the residual to a standard multivariate normal (MVN) distributed random variable by subtracting its total mean and subsequently dividing its total standard deviation (Hashemi & Ruths, 2019),

$$\mathbf{T}_g = \boldsymbol{\Sigma}^{-1/2} (\mathbf{r}_k - \boldsymbol{\mu}), \quad (49)$$

where $\boldsymbol{\mu}$ is the total mean and $\boldsymbol{\Sigma}^{-1/2}$ is the principal square root matrix of the total covariance ($\boldsymbol{\Sigma}$) of the residual, respectively. According to the law of total covariance (Weiss et al., 2006), $\boldsymbol{\mu}$ and $\boldsymbol{\Sigma}$ are given by

$$\boldsymbol{\mu} = \sum_{a=1}^{m_2} \sum_{b=1}^{m_2} \sum_{c=1}^{m_1} p_{abc} \boldsymbol{\mu}_{abc} \quad (50a)$$

$$\boldsymbol{\Sigma} = \sum_{a=1}^{m_2} \sum_{b=1}^{m_2} \sum_{c=1}^{m_1} p_{abc} \boldsymbol{\pi}_{abc} + (\boldsymbol{\mu} - \boldsymbol{\mu}_{abc})(\boldsymbol{\mu} - \boldsymbol{\mu}_{abc})^T. \quad (50b)$$

By setting the number of the Gaussian components of the GMM to one, the above transformation formulation can be easily extended to situations in which the residual is formulated as Gaussian distribution (Liu et al., 2017). \mathbf{T}_g can be interpreted as the standardized measurement residual vector, which is assumed to have a standard MVN distribution. The $2n \times 1$ vector \mathbf{T}_g can be written as

$$\mathbf{T}_g = [T_{g,1}, T_{g,2}, \dots, T_{g,2n}], \quad (51)$$

where $T_{g,1}, T_{g,2}, \dots, T_{g,2n}$ are assumed to be mutually independent standard normal random variables. We can construct the following test statistic t_g ,

$$t_g = \mathbf{T}_g^T \mathbf{T}_g = T_{g,1}^2 + T_{g,2}^2 + \dots + T_{g,2n}^2. \quad (52)$$

Since $T_{g,1}, T_{g,2}, \dots, T_{g,2n}$ are mutually independent, t_g follows the Chi-squared distribution with $2n$ DOF. The Chi-squared test for fault detection associated with the test statistic t_g at a given significance level α is

$$H_1 : t_g > TD_\alpha \quad (53a)$$

$$H_0 : t_g \leq TD_\alpha, \quad (53b)$$

where TD_α is determined by

$$P(t_g > TD_\alpha | H_0) = \alpha. \quad (54)$$

The significance level α can also be interpreted as the desired false alarm rate in the fault detection context when the assumption that \mathbf{T}_g has a standard MVN distribution is valid. However, the assumption is unrealistic in real-world applications. Therefore, criteria are required to examine the real performance of the fault detection results. In this study, two criteria, including the false alarm rate (FAR) and the fault detection rate (FDR) in a period, are formulated as

$$FAR = \frac{n_{FP}}{n_{FP} + n_{TN}} \quad (55a)$$

$$FDR = \frac{n_{TP}}{n_{TP} + n_{FN}}, \quad (55b)$$

where n_{TP} is the number of true positive epochs, n_{TN} is the number of true negative epochs, n_{FP} is the number of false positive epochs, and n_{FN} is the number of false negative epochs.

IV. EXPERIMENTAL RESULTS

1. Setup of The Experiments

To ensure the reproducibility of experiments and simulate Gaussian mixture model (GMM)-distributed noises, it is crucial to have a fully controllable environment for examining the proposed method's performance. In this study, we construct a simulated urban environment utilizing the 3D simulator, CARLA (Dosovitskiy et al., 2017). By employing both automatic and manual checks, we are able to generate a fault-free urban scenario. Additionally, we have the capability to inject specific faults at given times with user-defined settings. As shown in Figure 2(a), the simulated vehicle is equipped with seven 2D LiDARs and a simulated IMU sensor. The measurements of 2D LiDARs are simulated by the ray-cast technology, which can accurately reflect the actual position of the point hit by each laser beam. Users can add extra noises to the 2D LiDAR measurements. The simulated sensors can directly output readings of physical parameters (such as angular velocity and acceleration) of the vehicle through CARLA. Additional noises are incorporated into the readings with customized configurations, eventually simulating the IMU sensor. Recall Section II.2 that the 2D LiDAR measurement model requires pre-stored plane information. In the simulated platform, it is much easier to extract this information without introducing additional errors. We accomplish this by exporting the 3D objects in the simulated environment to Blender (Community, 2018), an open-source 3D modeling and rendering software, to extract the faces of all objects of interest, such as buildings, walls, and roads. As shown in Figure 2(b), the face (plane) information, including normal, center, and vertices, can be extracted correctly by automatic operation and manual checking in Blender.

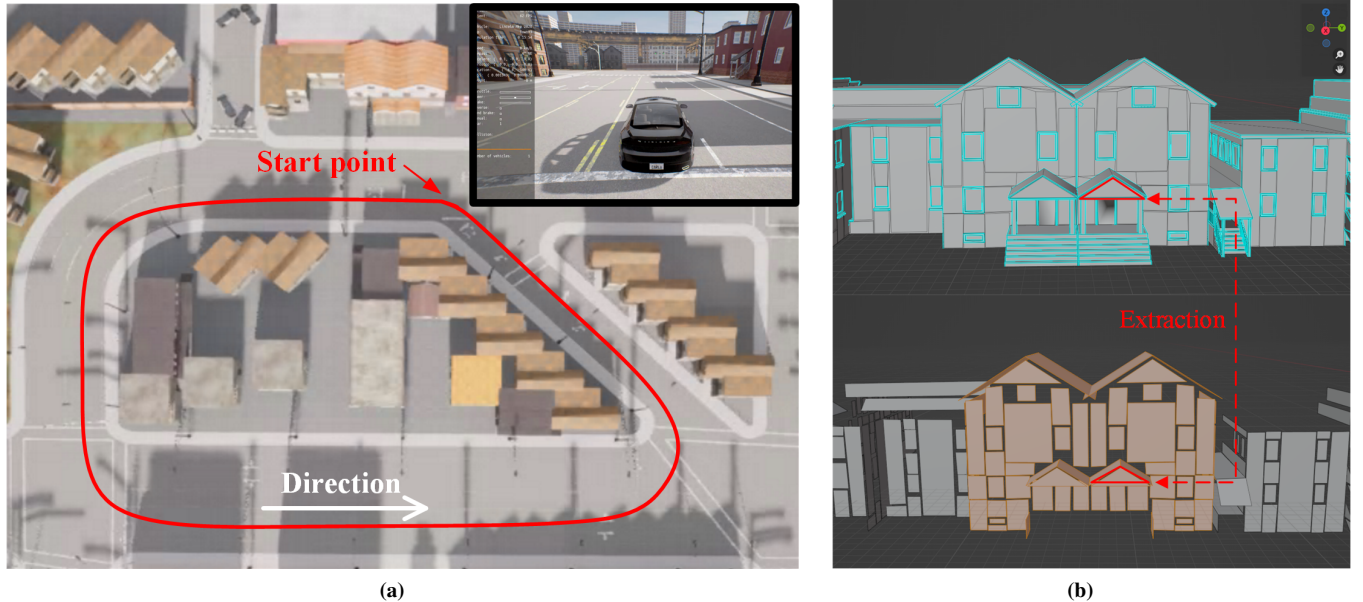


Figure 2: (a) The simulated urban environment constructed based on CARLA, where the designed track of the ground vehicle is marked as the red line. The thumbnail figure shows the simulated vehicle that can move along the road by manual control or programmed control. (b) A demonstration of face extraction for buildings in Blender.

Based on the constructed simulation platform, the simulated vehicle is programmed to move along the track in Figure 2(a) at a constant speed of 30 km/h. In the experiment, the output frequency of the LiDARs is 10 Hz, and LiDAR measurement noises $\eta_i = \begin{bmatrix} \tilde{\phi}_i & \tilde{\rho}_i \end{bmatrix}^T$ are configured to have the multivariate GMM distribution as follows:

$$f_{\eta_i}(\cdot) = p_1 \mathcal{N} \left(\begin{bmatrix} 0 \\ \mu_1 \end{bmatrix}, \begin{bmatrix} 0.0003^2 & 0 \\ 0 & \delta_1^2 \end{bmatrix} \right) + p_2 \mathcal{N} \left(\begin{bmatrix} 0 \\ \mu_2 \end{bmatrix}, \begin{bmatrix} 0.0003^2 & 0 \\ 0 & \delta_2^2 \end{bmatrix} \right), \quad (56)$$

where the bearing noise is set as zero-mean Gaussian with a standard deviation of 0.0003 rad, and the range noise is determined by $\mathbf{p} = [p_1, p_2]$, $\boldsymbol{\mu} = [\mu_1, \mu_2]$ and $\boldsymbol{\delta} = [\delta_1, \delta_2]$. In this experiment, we evaluate three settings of \mathbf{p} , $\boldsymbol{\mu}$ and $\boldsymbol{\delta}$, as shown in Table 1. In addition, a degraded case that the range noise is generated from a Gaussian distribution is also evaluated, as presented in Table 1. On the other hand, the probability density function of the process noise $\mathbf{v} = [\mathbf{n}_a^T, \mathbf{n}_g^T, \mathbf{n}_{wa}^T, \mathbf{n}_{wg}^T]^T$ is set as zero-mean multivariate Gaussian distribution, which are simulated based on the MEMS-based IMU (Devices, 2018). Specifically, the bias

Table 1: Settings of Range Noises of the LiDAR Measurement

Noise Setting	Mixture \mathbf{p}	Mean μ (m)	Std. δ (m)
NS1	[0.9,0.1]	[-0.01,0.03]	[0.02,0.06]
NS2	[0.8,0.2]	[-0.01,0.03]	[0.02,0.06]
NS4	[0.9,0.1]	[-0.01,0.03]	[0.03,0.04]
Gaussian	-	0	0.03

and the noise of the gyroscope measurement are set as $2^\circ/\text{hr}$ and $0.15^\circ/\text{hr}$, respectively, while the bias and the noise of the accelerator measurement are set as $3.6\ \mu\text{g}$ and $0.012\ \text{m/sec}/\sqrt{\text{hr}}$, respectively. The output frequency of the simulated IMU is 100 Hz.

To examine the strength of GMM noise modeling in fault detection tasks, we construct a baseline detector based on Gaussian noise modeling. Specifically, the measurement noise is modeled as zero-mean Gaussian noise, whose covariance is obtained by calculating the variance of samples generated from the noise distribution in Table 1 through the Monte-Carlo simulation. The residual transformation and the construction of the test statistic are similar to the process described in III.2. Therefore, the fundamental difference between this Gaussian approach and the proposed methods lies in the way of noise modeling.

2. Fault Detection Performance with Step Failure

In this section, we examine the performance of the proposed method in detecting step failures. We start the vehicle at time $t = 0\text{s}$ in a fault-free setting. At $t = 4\text{s}$, we inject a step failure with a magnitude of 0.1 m to one of the LiDAR range measurements. This fault persists for a duration of 16 s . Figure 3 shows the detection results of two methods with noise setting NS1 and the significance level of 0.05 . The plot depicts the difference between the chi-square test statistic and the threshold for each method over time. Recall the chi-squared test described in Section III.2. It is straightforward that a positive value indicates the detection of potential faults. During the fault injection period ($4 \sim 20\text{ s}$), the value of the proposed method is substantially larger than that of the Gaussian method, showing that the proposed method is more sensitive to faults. Furthermore, it is worth noting that the Gaussian method occasionally produces negative values at certain epochs during $14 \sim 20\text{ s}$, as marked by the green rectangular area. However, such occurrences are significantly infrequent in the proposed method, suggesting that the proposed method is more stable in detecting step failures. Just like every coin has two sides, the proposed methods exhibit a slight, yet increasing trend to classify normal measurements as faults. As shown in the figure, the proposed method produces slightly more positive values than the Gaussian method outside the fault injection period.

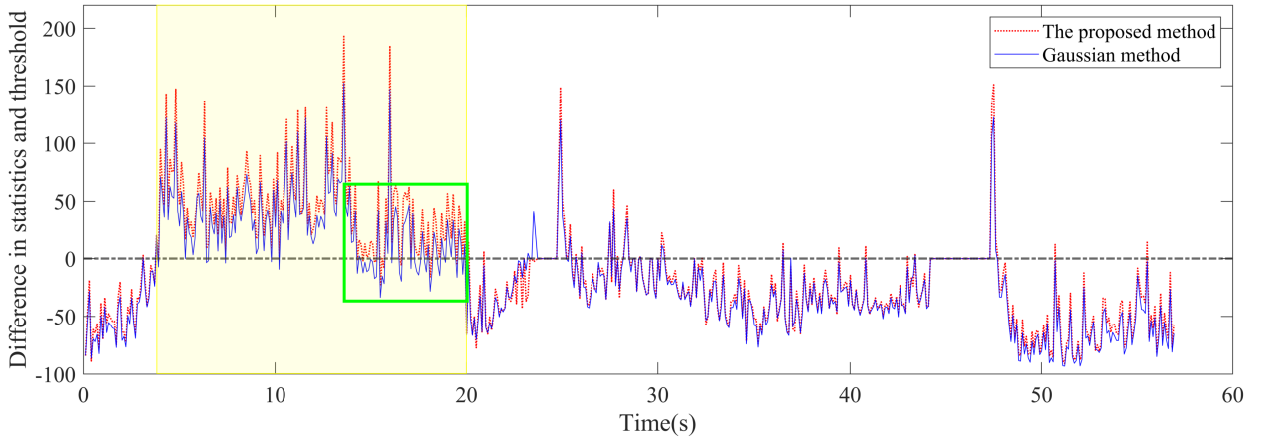


Figure 3: The difference between the chi-square test statistic and threshold against time in the step failure experiments with noise setting NS1 ($\alpha = 0.05$), where a positive value suggests the detection of faults. The shaded area shows the period of fault injection, i.e., $4 \sim 20\text{ s}$.

For a quantitative analysis, we calculate the fault detection rate (FDR) and false alarm rate (FAR) in the step failure experiment and present the results in Table 2 and Table 3, respectively. When the significance level α is set as 0.05 , the FDR of the proposed method exceeds 85% under each noise setting, which is significantly larger than that of the Gaussian method. Particularly within the noise setting NS2, the FDR of the total Gaussian-GMM method surpasses that of the Gaussian method by 30% ,

Table 2: Comparison of the Proposed Method with the Gaussian Method on Fault Detection Rate (FDR)

Range Noise Setting	Significance Level	Fault Detection Rate (FDR)	
		GMM Method	Gaussian Method
NS1	0.05	94.38	78.13
	0.01	85.00	71.88
	0.001	73.75	62.50
NS2	0.05	85.00	65.63
	0.01	72.50	52.50
	0.001	58.13	37.50
NS4	0.05	85.00	73.75
	0.01	71.88	60.63
	0.001	55.63	47.50
Gaussian	0.05	93.13	93.13
	0.01	68.75	68.75
	0.001	68.13	68.13

Table 3: Comparison of the Proposed Method with the Gaussian Method on False Alarm Rate (FAR)

Range Noise Setting	Significance Level	False Alarm Rate (FAR)	
		GMM Method	Gaussian Method
NS1	0.05	7.26	5.03
	0.01	4.47	2.79
	0.001	2.23	1.96
NS2	0.05	6.70	3.63
	0.01	3.07	1.40
	0.001	1.11	0.84
NS4	0.05	2.79	2.51
	0.01	1.68	1.40
	0.001	1.40	0.84
Gaussian	0.05	3.07	3.07
	0.01	2.23	2.23
	0.001	0.56	0.56

showing the most substantial improvement among all noise configurations. We also observe that the FDR for both methods decreases as the significance level increases. This observation is reasonable, as a higher significance level corresponds to a larger threshold in the chi-squared test. When looking at Table 3, we find that the FAR of the proposed method slightly increases but is still comparable to the Gaussian method in all noise settings at $\alpha = 0.05$. Since reducing the missed detection rate is typically prioritized over false positives for multi-sensor navigation systems, the sacrifice in FAR could be accepted to a certain extent. Similar results are observed when α is set as 0.01 and 0.001.

3. Fault Detection Performance with Slope Failure

In this section, we examine the performance of the proposed method in detecting slope failures, which are faults characterized by an increasing magnitude over time. Similar to the experimental process in Section IV.2, the vehicle is started at time $t = 0$ s in a fault-free setting. At $t = 34$ s, we inject a slope failure with a rate of 0.05 m/s to one of the LiDAR range measurements. The injection continues until $t = 44$ s. We first examine the detection performance of two methods under noise setting NS1.

Figure 4 plots the difference between the chi-square test statistic and the threshold for each method against time ($\alpha = 0.05$). During the injection period, both methods show an increasing trend in the difference value. After $3 \sim 4$ s, both methods yield a positive value, suggesting that a fault is declared. To assess the sensitivity of the detectors to slope failures, we analyze the delayed time of each method. The delayed time refers to the interval between the start of the fault injection and the first stable detected epoch. In other words, it is the duration during which the subsequent diagnosis consistently declares a fault throughout the remaining injection period. As shown in the thumbnail image in the plot, the stable detected epoch of the proposed method is 37.5 s, indicating that the delayed time of the proposed method is 3.5 s. However, the detection performance of the Gaussian method is not as stable as the proposed method. Although the Gaussian method has detected a fault at as early as $t = 37.6$ s, the subsequent diagnosis results are not consistent before $t = 38.6$ s. As shown in the thumbnail figure, the Gaussian method yields a negative difference value at two timestamps during $37.6 \sim 38.6$ s, as marked by the green circles. It is until $t = 38.6$ s that the detection results of the Gaussian method become stable, suggesting a delayed time of 4.6 s. Table 4 lists the delayed time of the two methods under different noise settings with $\alpha = 0.05$. It is shown that the delayed time of the proposed method is reduced by 17 ~ 23% compared to the Gaussian method under all noise settings, suggesting that the proposed method is more sensitive to slope failures. In the Gaussian noise setting, the proposed method degrades to the Gaussian method, yielding the same delayed time.

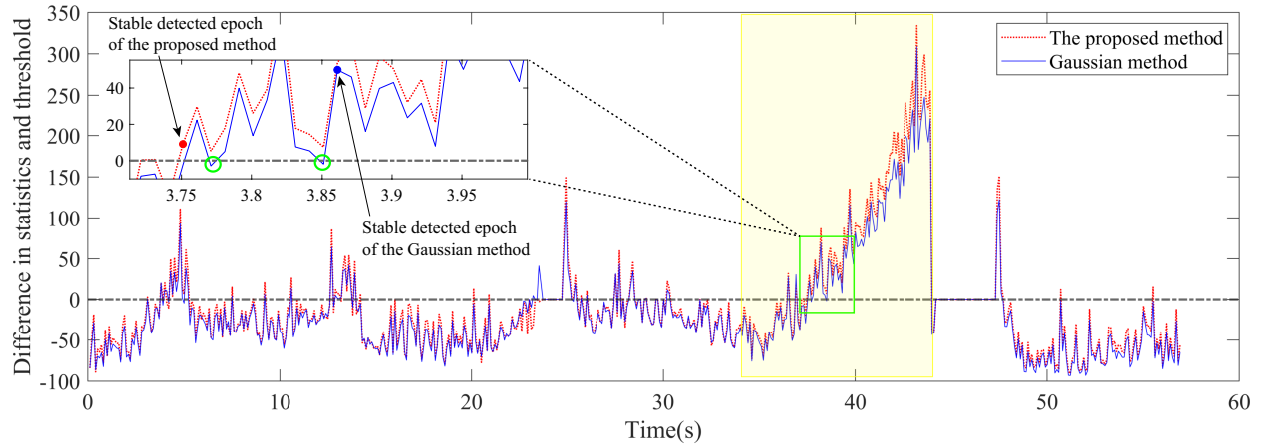


Figure 4: The difference between the chi-square test statistic and threshold against time in the slope failure experiments with noise setting NS1 ($\alpha = 0.05$), where a positive value suggests the detection of faults. The shaded area shows the time period of fault injection, i.e., $34 \sim 44$ s.

Table 4: Comparison of the Proposed Method with the Gaussian Method on Delayed Time ($\alpha = 0.05$)

Range Noise Setting	GMM Method	Gaussian Method
NS1	3.5 s	4.6 s
NS2	4.2 s	5.3 s
NS4	4.3 s	5.2 s
Gaussian	5.3 s	5.3 s

V. CONCLUSION

In this work, we propose a fault detection algorithm for an EKF-based LiDAR/IMU integrated localization system when measurement noises are characterized by non-Gaussian distributions. We adopt the Gaussian mixture model (GMM) to model the nominal errors in LiDAR measurements. With a comprehensive analysis of the measurement residual in the EKF system, we establish the relationship between GMM-distributed noises and the residual, showing that the residual is the linear combination of process noises and measurement noises. Consequently, we obtain the profile of the residual, which is proved to be GMM distributed. Based on the law of total variance, we transform the GMM-distributed residual to a Gaussian-like variable, and take its Mahalanobis distance to the standard normal distribution to construct a test statistic. Finally, we employ the chi-square test based on the constructed test statistic to detect potential faults in the measurements.

We evaluate the proposed method in a simulated urban environment constructed based on Carla, which provides a fault-free environment and enables the injection of faults at a given time. In the step failure experiment, the proposed method yields over

85 % fault detection rate (FDR) on all three GMM noise settings, which significantly outperforms the Gaussian method. In the slope failure experiment, the delayed time of the proposed method is reduced by 17 ~ 23 % compared to the Gaussian method under all noise settings, demonstrating the greater sensitivity of the proposed method in detecting slowly increasing faults. Since the fundamental difference between the proposed method and the Gaussian method lies in the way of noise modeling, these experimental results imply that utilizing GMM-based noise modeling can be beneficial for fault detection tasks in localization systems with non-Gaussian noises, encouraging researchers to explore this direction.

REFERENCES

- Blanch, J., Walter, T., Enge, P., Lee, Y., Pervan, B., Rippl, M., & Spletter, A. (2012). Advanced raim user algorithm description: Integrity support message processing, fault detection, exclusion, and protection level calculation. *Proceedings of the 25th International Technical Meeting of The Satellite Division of the Institute of Navigation (ION GNSS 2012)*, 2828–2849.
- Community, B. O. (2018). *Blender - a 3D modelling and rendering package*. Blender Foundation. Stichting Blender Foundation, Amsterdam. <http://www.blender.org>
- Daum, F. (2005). Nonlinear filters: Beyond the Kalman filter. *IEEE Aerospace and Electronic Systems Magazine*, 20(8), 57–69. <https://doi.org/10.1109/MAES.2005.1499276>
- Davis, B., & Blair, W. D. (2015). Gaussian mixture approach to long range radar tracking with high range resolution. *2015 IEEE Aerospace Conference*, 1–9. <https://doi.org/10.1109/AERO.2015.7119222>
- Devices, A. (2018). ADIS16465: Precision MEMS IMU module data sheet (Rev. C). <https://www.analog.com/media/en/technical-documentation/data-sheets/ADIS16465.pdf>
- Dosovitskiy, A., Ros, G., Codevilla, F., Lopez, A., & Koltun, V. (2017). CARLA: An open urban driving simulator. *Conference on robot learning*, 1–16.
- Gao, Z., Ding, S. X., & Cecati, C. (2015). Real-time fault diagnosis and fault-tolerant control. *IEEE Transactions on Industrial Electronics*, 62(6), 3752–3756. <https://doi.org/10.1109/TIE.2015.2417511>
- Hashemi, N., & Ruths, J. (2019). Generalized Chi-squared detector for LTI systems with non-Gaussian noise. *2019 American Control Conference (ACC)*, 404–410. <https://doi.org/10.23919/ACC.2019.8815139>
- Hesch, J. A., Mirzaei, F. M., Mariottini, G. L., & Roumeliotis, S. I. (2010). A laser-aided inertial navigation system (L-INS) for human localization in unknown indoor environments. *2010 IEEE International Conference on Robotics and Automation*, 5376–5382. <https://doi.org/10.1109/ROBOT.2010.5509693>
- Joerger, M., Chan, F.-C., & Pervan, B. (2014). Solution separation versus residual-based RAIM. *NAVIGATION*, 61(4), 273–291. <https://doi.org/10.1002/navi.71>
- Kaplan, E. D., & Hegarty, C. (Eds.). (2006). *Understanding GPS: Principles and applications* (2nd ed.). Artech house.
- Lefferts, E., Markley, F., & Shuster, M. (1982). Kalman filtering for spacecraft attitude estimation. *Journal of Guidance, Control, and Dynamics*, 5(5), 417–429. <https://doi.org/10.2514/3.56190>
- Liu, C., Wang, H., Li, N., & Yu, Y. (2017). Sensor fault diagnosis of GPS/INS tightly coupled navigation system based on state Chi-square test and improved simplified fuzzy ARTMAP neural network. *2017 IEEE International Conference on Robotics and Biomimetics (ROBIO)*, 2527–2532. <https://doi.org/10.1109/ROBIO.2017.8324800>
- Pervan, B. S., Pullen, S. P., & Christie, J. R. (1998). A multiple hypothesis approach to satellite navigation integrity. *NAVIGATION*, 45(1), 61–71. <https://doi.org/10.1002/j.2161-4296.1998.tb02372.x>
- Puchalski, R., & Giernacki, W. (2022). UAV fault detection methods, state-of-the-art. *Drones*, 6(11), 330. <https://doi.org/10.3390/drones6110330>
- Rife, J. H. (2018). Overbounding risk for quadratic monitors with arbitrary noise distributions. *IEEE Transactions on Aerospace and Electronic Systems*, 54(4), 1618–1627. <https://doi.org/10.1109/TAES.2018.2798258>
- Vargas, J., Alsweiss, S., Toker, O., Razdan, R., & Santos, J. (2021). An overview of autonomous vehicles sensors and their vulnerability to weather conditions. *Sensors*, 21(16), 5397. <https://doi.org/10.3390/s21165397>
- Vargas Rivero, J., Gerbich, T., Buschardt, B., & Chen, J. (2022). The effect of spray water on an automotive LIDAR sensor: A real-time simulation study. *IEEE Transactions on Intelligent Vehicles*, 7(1), 57–72. <https://doi.org/10.1109/TIV.2021.3067892>
- Walter, T., & Enge, P. (1995). Weighted RAIM for precision approach. *Proceedings of the 8th International Technical Meeting of the Satellite Division of The Institute of Navigation (ION GPS 1995)*, 1995–2004.
- Weiss, N., Holmes, P., & Hardy, M. (2006). *A course in probability*. Pearson Addison Wesley. <https://books.google.com.hk/books?id=Be9fJwAACAAJ>
- Yun, Y., Yun, H., Kim, D., & Kee, C. (2008). A Gaussian sum filter approach for DGNSS integrity monitoring. *The Journal of Navigation*, 61(4), 687–703. <https://doi.org/10.1017/S0373463308004906>
- Zhao, S., & Farrell, J. A. (2013). 2d LIDAR aided INS for vehicle positioning in urban environments. *2013 IEEE International Conference on Control Applications (CCA)*, 376–381. <https://doi.org/10.1109/CCA.2013.6662778>